PHYSICAL REVIEW D VOLUME 32, NUMBER 3 1 AUGUST 1985

Measurement of the rate for pion beta decay

W. K. McFarlane, L. B. Auerbach, F. C. Gaille,* V. L. Highland, and E. Jastrzembski†
Physics Department, Temple University, Philadelphia, Pennsylvania 19122

R. J. Macek, F. H. Cverna, C. M. Hoffman, G. E. Hogan, R. E. Morgado, J. C. Pratt, and R. D. Werbeck
Los Alamos National Laboratory, Los Alamos, New Mexico 87545

(Received 2 November 1984)

The conserved-vector-current hypothesis, together with measured nuclear beta-decay rates, predicts a value of the rate for the decay $\pi^+ \rightarrow \pi^0 e^+ \nu$ of $0.4027 \pm 0.0018\ \mathrm{s}^{-1}$. Using a decay-in-flight technique we have made the most precise measurement to date of this rate, obtaining the value $0.394 \pm 0.015\ \mathrm{s}^{-1}$, in good agreement with the prediction. This differs slightly from the value previously reported in W. K. McFarlane *et al.*, Phys. Rev. Lett. 51, 249 (1983).

I. INTRODUCTION

We present here an expanded description of a measurement[1] of the rate for pion beta decay ($\pi\beta$), $\pi^+ \rightarrow \pi^0 e^+ \nu$, made using a new technique at the Clinton P. Anderson Meson Physics Facility (LAMPF), that is substantially more precise than previous measurements. According to the conserved-vector-current (CVC) hypothesis,[2] a cornerstone of the unified theory of electromagnetic and weak interactions, the rate for pion beta decay is directly related to the ft value for nuclear beta decay.

Following Sirlin[3] and Källén,[4] the inverse lifetime $1/\tau$ for pion beta decay can be written

$$\frac{1}{\tau_0} = \frac{G_{\beta V}{}^2}{30\pi^3} \left[1 - \frac{\Delta}{2m_+} \right]^3 \Delta^5 F(\epsilon, \Delta) \, , \tag{1.1}$$

$$\frac{1}{\tau} = \frac{1}{\tau_0}(1+\delta_\pi) \, , \tag{1.2}$$

where τ_0 is the lifetime in the absence of radiative corrections, $G_{\beta V}$ is the weak-interaction coupling constant for pure vector beta decay, Δ is the $\pi^+ - \pi^0$ mass difference, m_+ is the π^+ mass, and the function F is close to unity ($\epsilon = m_e/\Delta$, m_e being the electron mass). The observed lifetime τ is obtained from τ_0 by using the radiative correction δ_π. The function F is

$$F(\epsilon,\Delta) = \sqrt{1-\epsilon} \left[1 - \frac{9\epsilon}{2} - 4\epsilon^2 \right] + \tfrac{15}{2}\epsilon^2 \ln \left[\frac{1+\sqrt{1-\epsilon}}{\sqrt{\epsilon}} \right] - \frac{3}{7} \left[\frac{\Delta}{m_+ + m_0} \right]^2 , \tag{1.3}$$

where m_0 is the π^0 mass.

The half-life $t_{1/2}$ for nuclear beta decay is given (in the absence of radiative corrections) by

$$\frac{1}{t_{1/2}} = \frac{G_{\beta V}{}^2 m_e{}^5}{\pi^3} f \, , \tag{1.4}$$

where f is a phase-space factor. Converting to the lifetime t and including a factor for radiative corrections gives

$$G_{\beta V}{}^2 = \frac{\pi^3}{m_e{}^5} \frac{\ln 2}{(ft)_N} (1+\delta_N)^{-1} \, , \tag{1.5}$$

where δ_N is the radiative correction for the nuclear decay considered and $(ft)_N$ is the measured ft value. The CVC hypothesis is that $G_{\beta V}$ is the same in Eqs. (1.1) and (1.5), so combining with Eq. (1.2) gives

$$\frac{1}{\tau} = \frac{\ln 2}{30(ft)_N} \left[\frac{\Delta}{m_e} \right]^5 \left[1 - \frac{\Delta}{2m_+} \right]^3 \times F(\epsilon,\Delta)(1+\delta_\pi)(1+\delta_N)^{-1} \, . \tag{1.6}$$

In the Weinberg-Salam (WS) model[5] as applied by Sirlin[3] the electroweak corrections are the same for pion and nuclear beta decays, except for a small energy-release-dependent correction[6] δ^0. The ft value normally quoted, ft', is corrected only for this "outer" radiative correction δ^0 and contains the inner correction δ^i, i.e.,

$$ft = (ft)_N(1+\delta_N^i+\delta_N^0) = ft'(1+\delta_N^i) \, . \tag{1.7}$$

Thus, since $\delta_\pi = \delta_\pi^i + \delta_\pi^0$ and $\delta_\pi^i = \delta_N^i = \delta^i$ we obtain

$$\frac{1}{\tau} = \frac{\ln 2}{30(ft')} \left[\frac{\Delta}{m_e} \right]^5 \left[1 - \frac{\Delta}{2m_+} \right]^3 F(\epsilon,\Delta)(1+\delta_\pi^0) \, . \tag{1.8}$$

Using the numerical values in Table I, Eq. (1.8) gives

$$1/\tau = 0.4027 \pm 0.0018\ \mathrm{s}^{-1} \, , \tag{1.9}$$

and, using the pion lifetime,[9] we calculate a branching ratio for pion beta decay relative to all pion decays of

$$(1.0482 \pm 0.0048) \times 10^{-8} \, . \tag{1.10}$$

The small uncertainty in this precise prediction is primarily due to the uncertainty in Δ.

The most precise previous experiment was that of Depommier *et al.*,[10] who found a branching ratio $\pi\beta/(\pi^+ \rightarrow \mu^+ + \nu)$ of $(1.00^{+0.08}_{-0.10}) \times 10^{-8}$, corresponding to a decay rate of $0.38^{+0.03}_{-0.04}\ \mathrm{s}^{-1}$. Though this result is consistent with the theory, it is very desirable to improve the experimental precision since the pion-beta-decay rate is the most direct test of the CVC hypothesis.

TABLE I. Data for expected-rate and branching-ratio calculation.

Factor	Value	Ref.
ft'	3083.4 ± 3.0 s	7,8
Δ	4.6043 ± 0.0037 MeV	9
m_0	134.9630 ± 0.0038 MeV	9
m_+	139.5673 ± 0.0007 MeV	9
m_e	$0.511\,003\,4\pm0.000\,001\,4$ MeV	9
δ_π^0	0.0105 ± 0.0015	6
t_π	$(26.030\pm0.023)\times10^{-9}$ s	9

II. DESCRIPTION OF APPARATUS

In contrast to the previous experiments, which used stopped pions, this one used decays in flight of a π^+ beam, of momentum 522.1 ± 0.8 MeV/c, and intensity 2×10^8 pions/s. The beam was the P^3 beam at LAMPF,[11] where pions were produced by 790-MeV protons incident on the $A2$ target. The P^3 beam had two bends with an intermediate focus, and a degrader placed at this focus gave partial separation of pions from protons. The π^0 from the π^+ decay had transverse momentum less than 5 MeV/c and nearly the same momentum in the laboratory as the π^+; we detected the γ rays from the π^0 decay. Figure 1 shows our apparatus, in which a decay region was defined by the minimum opening angle between the γ's and the geometrical limits of two γ detectors. The π^0 had a mean total energy of about 523 MeV and the energy of geometrically detectable coincident γ's ranged from 175 to 350 MeV. To avoid background from pion charge exchange, the decay region was in a vacuum tank at 3×10^{-7} Torr. The beam was collimated twice and the γ detectors (as well as a pair of electron detectors) were located outside the 5° cone filled by the intense flux of muons from decay of the charged pions. The second collimator was toroidally magnetized to reduce muon scattering into the detectors. A system of beam monitors was placed downstream, as described below.

The decay rate R is found from

$$N_\beta = R N_\pi P^2(\beta\gamma c)^{-1}\int \eta(z)dz \prod_{i=1}^{4} F_i \,, \tag{2.1}$$

where N_β is the number of accepted events, N_π is the number of beam pions entering the apparatus, P^2 is the joint γ-ray conversion probability, $(\beta\gamma c)^{-1}$ is the proper time of the pion per unit flight path, $\eta(z)$ is the geometric efficiency of detection as a function of position z along the beam, and the four factors F_i are corrections. The combination

$$T=(\beta\gamma c)^{-1}\int \eta(z)dz \tag{2.2}$$

is the effective proper time spent by a beam pion in the decay region, and was determined by a Monte Carlo program, PIOBETA (see Sec. VI C). The parameter T is given later (in Table IX) along with the other factors entering into the decay-rate calculations, which are described in detail below.

Two points about our experimental arrangement should be noted. First, the design of the experiment is such that the rate calculation is independent of the beam momentum to a good approximation: the parameter T is composed of two factors which depend on pion momentum in opposite ways [the integral of $\eta(z)$ is approximately proportional to γ, because the minimum opening angle for the π^0 decay is inversely proportional to γ]. Second, while the efficient detection of γ rays is easier the higher their energy, if the primary beam were to have an energy above kaon production threshold, the resulting backgrounds from K_{e3}^+ decays would be difficult to deal with. Hence the choice of LAMPF (despite its low duty factor) and the choice of the highest pion energy available with good intensity.

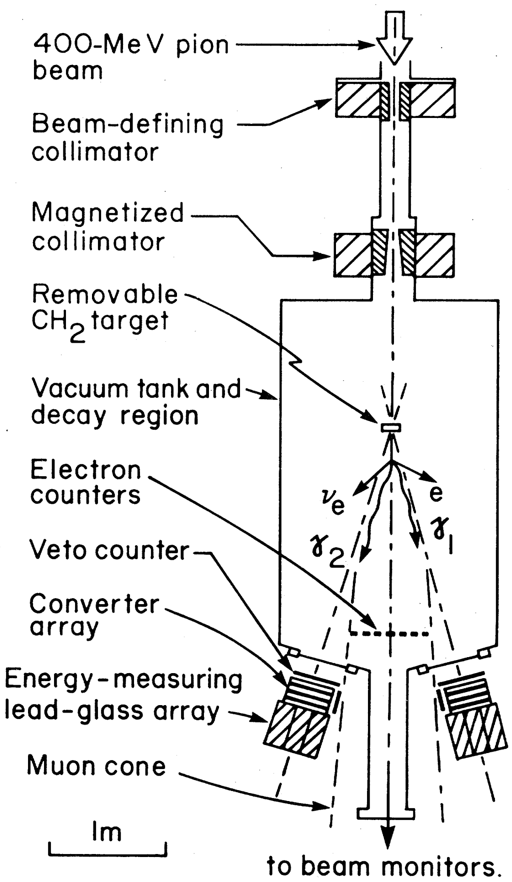

FIG. 1. Diagram of pion-beta-decay detection apparatus.

A. The collimation system

The upstream collimation system (Fig. 1) consisted of a beam-defining and a "magnetic" collimator, which were connected to the last quadrupole of the P^3 beam channel and to the vacuum tank, so that there were no windows between the beam-line vacuum and the decay region. A system of bellows allowed independent alignment of the two collimators.

The upstream collimator was a beam-defining collimator made of lead. It had an 8.89-cm-diameter bore, was 34.3 cm long, and was surrounded by a lead-iron shield.

The second collimator, called the magnetic collimator, was designed and built specifically for the experiment. One of the major difficulties of the experiment was to reduce random backgrounds to a level low enough to obtain a clear pion-beta-decay signal; a known source of background was muon scattering from the final collimator which could give some apparent neutral triggers. In a previous trial run, a passive collimator did not function well, so that a collimator with a toroidal magnetic field designed to trap positive particles was built.

According to a Monte Carlo study of an ideal collimator, which considered ionization loss and Molière scattering[12,13] of muons (program MUSCAT), a magnetic field of 2.0 T inside the collimator material could reduce by a factor of about 40 the rate of scattered muons hitting the two γ detectors. The final design of the magnetic collimator is shown in Fig. 2; in both *Oxz* and *Oyz* planes the shape of a section is an arc of a circle followed by a 5° slope. The actual device approximated this ideal curve in a piecewise fashion, and the collimator was made of silicon steel with an inner 20-mm-thick layer of the alloy Supermendur (50% iron, 48% Co, 2% C, Ni, Mn, Mo, Si, S, V), chosen for its high saturation field. The aperture was 7.6 by 20.3 cm^2 and the length 34 cm. Thin aluminum conductors on the inner faces made up a four-turn coil, to provide the magnetizing field. In the final assembly a current I of 25 A (about the maximum allowed by heating effects) produced an average magnetic field of 1.62 T in the core.

Tests were carried out to determine the background-reducing efficiency of the magnetic collimator. With $I=25$ A, the neutral-trigger background rates in each arm of the π^0 spectrometer were reduced by a factor of about 1.5 relative to the $I=0$ rate. This gave a factor of 2 reduction of the overall two-arm coincidence rate, which allowed us to take pion-beta-decay data at an average beam intensity almost twice as high as that which would have been possible without the magnetic field induced in the collimator. The remaining backgrounds came from pion charge exchanges in the collimator and in the material of the tank downstream of the detectors, and from neutrons.

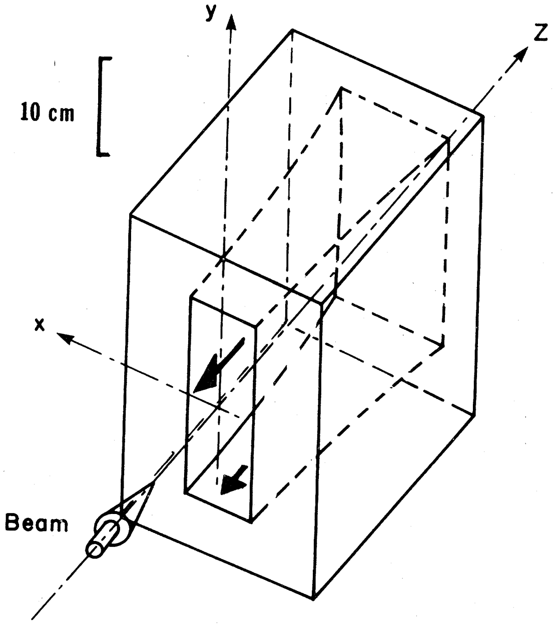

FIG. 2. Shape of the magnetic collimator. The field was produced by current sheets on the inside surfaces, indicated by the solid arrows.

B. The gamma detectors

The two γ detectors were modifications of the LAMPF π^0 spectrometer.[14] Each detector had three successive lead-glass counters as γ converters [0.56 radiation lengths (r.l.) each], followed by lead-glass blocks (14 r.l.) for total-energy measurement. Each converter was followed by two scintillation hodoscopes for position and time measurement. On each side, the hodoscopes defined a fiducial area with a surrounding guard ring. Veto counters in front and on the beam side rejected events with charged particles entering either detector. Figure 3 shows an expanded view of one arm of the detector. The converters were made from five slabs of glass side-by-side and viewed end-on. The scintillator hodoscopes were 12.7-mm-thick X and Y arrays. In the central fiducial region the counters were 150 mm wide (two X counters and four Y counters); two counters on each edge of each array were 30 mm wide. The total area covered by the scintillators was slightly larger in the horizontal (X direction) than the converters, but the fiducial area was entirely inside the glass, and aluminum bars of approximately the same equivalent conversion thickness were placed on each side of the converters to ensure constant conversion efficiency across the entire scintillator area. The method of wrapping and mounting the scintillators minimized the spaces between them, to less than 0.5 mm. The final positions of the scintillator edges, which define our acceptance, were surveyed to better than 1 mm precision.

The gains of the photomultipliers (PM's) viewing the lead glass were stabilized by the use of sources embedded in small scintillators at the far end of each block; "source" data were taken regularly during each run and used to modify calibration constants established in an earlier run using a 270-MeV/c electron beam. Pulse-height and time spectra of all scintillation counters were accumulated online and were used to maintain proper operation of the hodoscopes.

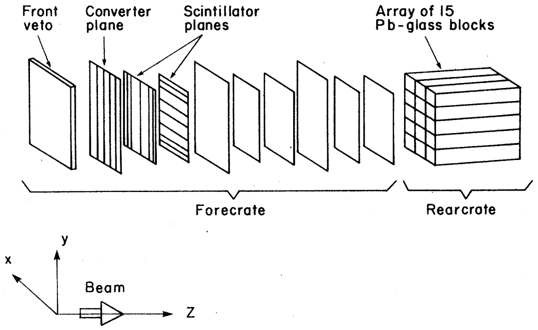

FIG. 3. Expanded view of one γ detector. The side veto is not shown.

Scintillation counters were also installed inside the vacuum tank to detect the decay electron (in about 10% of the decays); they did not overlap in solid angle with the γ detectors.

C. Trigger electronics

The trigger logic, sketched in Fig. 4, required a coincidence between neutral particles converting in the two detectors, and a minimum energy deposition of 40 MeV in each detector. A neutral conversion was signaled by a coincidence between an X and a Y hodoscope behind at least one of the three converters, with no signal in either the front or the side veto counter. The analog signals from all the lead-glass elements of each arm were added to form a pulse whose height depended on the total energy. This pulse was discriminated and a coincidence with the scintillators formed. Finally, a coincidence between the two arms was made.

The choice of resolving times (typically 20—30 ns) was a compromise between high efficiency and low dead times. Instantaneous rates in the veto counters were as high as 1 MHz, with dead time of the order of 10%, when using overlaps of 30—40 ns.

D. Data acquisition

The final pion-beta-decay data consisted of 667 000 events recorded on magnetic tape via a CAMAC system using the LAMPF Q data-acquisition package.[11] All scintillation times and pulse heights were recorded (whether involved in the trigger or not), as were lead-glass pulse heights and the times of the final lead-glass discriminators. Scales containing monitor information were recorded at regular intervals.

Beam intensities were varied to estimate dead-time effects. Pion-beta-decay data were taken at beam intensities ranging from 1×10^8 to 3×10^8 π/s (average), giving trigger rates of around 0.5 event/s. During calibration runs, the beam was reduced as needed to keep rates and data-acquisition dead-time below the 1% level: π^+CH_2 data were taken with a beam intensity of 2.6×10^7 π/s (average) (trigger rate 3.6 events/s) and π^-CH_2 at 3×10^6 π/s. The duty factor at LAMPF was 6—8 % during this experiment.

As will be discussed later, the data were analyzed in stages. The first stage selected candidate events (about 2% of the raw events) and wrote them onto eight summary tapes (ST's). Many of the corrections discussed below were made by summary tape (i.e., correction factors were found for each ST, rather than for individual runs or the data sample as a whole).

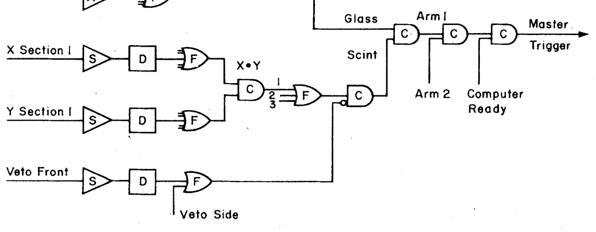

FIG. 4. Master trigger logic diagram. The signal "Stab" is used in the gain-stabilization process.

III. BEAM MONITORS AND BEAM CHARACTERISTICS

Figure 5 shows the layout of the beam-monitoring system placed downstream of the vacuum tank. It consisted of the following components: (i) the $\pi_{\mu2}$ monitor and its lead-brick shield, (ii) a lead collimator, (iii) an assembly of ionization chambers (11-in. IC), (iv) two scintillation counters S_1 and S_2, (v) an ionization chamber (TUIC), and (vi) two scintillation counters TB1 and TB2.

The beam-monitoring problem can be divided into two distinct and independent subproblems:

(a) The determination of the constant of proportionality between the number of pions in the beam and the number of counts from each monitor (below, we call this the multiplier for that monitor).

(b) The determination of the corrections affecting the beam monitors, as a function of time throughout the experiment.

The three beam monitors used were components (i), (iii), and (v) above, which were calibrated by comparison with a direct particle count from the counter telescope, component (iv). Corrections for beam contamination used information from the counters of item (vi).

Note that Z_0, the reference position along the beam line at which the total number of pions N_π is calculated from the reading of each monitor, corresponds physically to the starting point at which the pion beam is generated in the Monte Carlo program PIOBETA.

A. The lead collimator and scintillation counters

The collimator was made of lead and steel with a length of 33 cm and a bore 20.3 cm in diameter. Its purpose was to reduce the beam halo (mostly muons from upstream $\pi^+\rightarrow\mu^+\nu_\mu$ decays), so that the resulting particle flux was inside the apertures of the two ionization chambers and the two pairs of scintillators.

The scintillation counters S_1 and S_2 consisted of two identical Pilot U scintillators ($30.5\times30.5\times0.953$ cm^3) viewed by Amperex XP2020 PM's, operated in coincidence. This telescope provided a direct count of the beam particles so as to calibrate the three beam monitors. This could be done accurately only at low average beam intensity (about 10^5 π/s).

The scintillation counters, TB1 and TB2, each consisted of a NE102 scintillator ($36.3\times30.5\times0.953$ cm^3) on an EMI 2-in. PM. Their purpose was to sample the beam

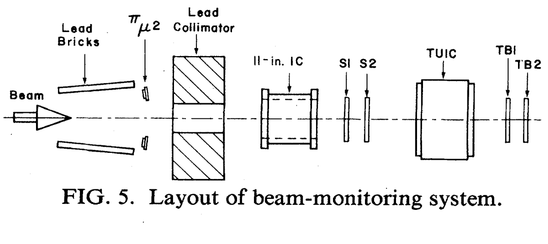

FIG. 5. Layout of beam-monitoring system.

composition (beam contamination) by time-of-flight (TOF) measurements, relative to the accelerating rf waveform, as described in Secs. III D and IV C below.

B. The $\pi_{\mu2}$ monitor

The $\pi_{\mu2}$ monitor consisted of two small scintillation counter coincidence telescopes placed symmetrically above and below the beam line in a vertical plane. Each telescope consisted of a smaller ($1.50\times1.50\times0.55$ cm^3) and a larger ($1.75\times1.75\times0.55$ cm^3) NE102 plastic scintillator, viewed by XP2230 PM's, centered relative to each other and placed closely one behind the other. The monitor was used to measure the absolute pion beam flux by counting muons coming from the $\pi_{\mu2}$ ($\pi^+\rightarrow\mu^+\nu_\mu$) decay mode of beam pions.

The symmetric geometry ensured a total counting rate nearly independent of vertical beam motions.[15] As shown in Fig. 5 two lead shields were placed upstream from the $\pi_{\mu2}$ monitor at an angle of about 3° relative to the beam line. These shields protected the $\pi_{\mu2}$ monitor from particles scattered upstream and helped to limit the range of detection along the beam axis. The telescope geometry (height, angle, etc.) was appropriate for detecting muons produced in $\pi_{\mu2}$ decays downstream from the magnetic collimator (see Fig. 1). The dimensions were chosen to give a counting rate of about 30 kHz in each telescope at the full average beam intensity of about 2×10^8 pions/s.

The number of pions in the beam is proportional to the sum of the number of counts in the top and bottom telescope of the $\pi_{\mu2}$ monitor. Including correction factors, one can write the following relation

$$N_\pi(Z_0)=M_p(T+B)_{\mathrm{cor}}\ , \tag{3.1}$$

$$(T+B)_{\mathrm{cor}}=(T+B)(1-C_{\mathrm{AC}})(1+C_{\mathrm{DT}})(1+C_{\mathrm{asy}})\ . \tag{3.2}$$

Here

$N_\pi(Z_0)$ = number of pions in the beam at Z_0 along the beam line;

M_p = multiplier for the $\pi_{\mu2}$ monitor at Z_0;

T = number of counts in the upper scintillator pair;

B = number of counts in the lower scintillator pair;

C_{AC} = accidental count correction;

C_{DT} = dead-time correction;

C_{asy} = asymmetry correction due to beam steering.

All these parameters are described and determined numerically in the next two sections.

C. The ionization chambers

Two ionization chambers (IC's) were used, both filled with research-grade argon gas (99.9995% pure) at roughly the atmospheric pressure of Los Alamos (11.3 psi). The downstream chamber (TUIC) had three identical parallel electrode plates (30.5×30.5 cm^2) made of 1 mil (0.025 mm) aluminum foil separated by 2.54 cm. The central electrode collects negative ions and was connected to the input of a Keithley 610CR electrometer. The two outer plates were connected to a high-voltage supply. The chamber was operated in "saturation," that is, the voltage was high enough that the ions created by the incident ionizing beam particles were collected on the plates without measurable recombination. The electrometer output was fed to a Vidar voltage-to-frequency converter (VFC), whose pulse output was counted in CAMAC scalers.

The upstream (11-in. IC) assembly had many circular electrode plates (0.025-mm-thick aluminum foil) configured as several sequential IC's using a common high-voltage supply in the same gas-filled cavity. In order along the beam they were as follows.

(i) "Thick," consisting of four gaps (two signal planes) having a total thickness of 101.5 mm.

(ii) "Thin," consisting of four gaps (two signal planes) having a total thickness of 18.4 mm.

(iii) "*L*-*R*," consisting of a split signal electrode in its own gap. The electrode was cut by a narrow vertical slit to form two independent D-shaped electrodes labeled *L* for left and *R* for right.

(iv) "*U*-*D*," consisting of another split electrode in an independent gap. It was cut by a narrow horizontal slit which formed two D-shaped electrodes *U* (up) and *D* (down).

The electronics for the thick and thin IC's consisted of electrometers and VFC's which were tested for linearity and calibrated by high-precision current sources. The outputs were available both as highly filtered dc voltages and as pulse trains which were counted in CAMAC scalers. The electrode signals from each split ion-chamber pair were routed to analog circuits which gave an analog output proportional to the normalized difference, e.g., $(L-R)/(L+R)$.

The narrow slits in the split-electrode chambers were aligned on the nominal beam line. Data from the split IC's were used to monitor the position of the beam centroid. When the beam misalignment exceeded tolerances of about 2 mm the beam was steered to realign the beam centroid.

The ratio of thin IC to thick IC was used to detect the onset of recombination of positive and negative ions before collection. In the absence of recombination effects the ratio should be a constant independent of beam intensity and be given by the ratio of the two chamber thicknesses. The thick IC (which has a lower collection field) would be the first to show reduced gain because of recombination. No evidence for such effects was observed during the course of this experiment.

The number of pions N_π in the beam measured by the ith IC at a point Z_i along the beam line, is given by

$$N_\pi(i)=S_i\frac{1}{\left[1+\sum_j G_j\langle R_j\rangle\right]}\frac{W_i}{K_iD_i\rho_0}\frac{1}{(dE/dX)_\pi}\frac{TP_{0i}}{T_0P_i}\ , \tag{3.3}$$

where

$N_\pi(i)$ = number of pions in the beam as measured by the ith IC at Z_i;

S_i = number of read-out counts from the ith IC;

$G_j=N_j(i)/N_\pi(i)$;

$N_j(i)$ = number of particles of species j at the ith IC;

$R_j=(dE/dX)_j/(dE/dX)_\pi$;

W_i = energy deposited per ion pair formed for the ith IC;

K_i = number of electrometer counts per elementary electric charge collected (i.e., per ion pair) from the *i*th IC;

D_i = active distance between the electrodes of the *i*th IC;

ρ_0 = density of the Ar gas at T_0 and P_{0i} of the *i*th IC;

T_0, P_{0i} = temperature and pressure at which the *i*th IC was calibrated;

T, P_i = temperature and pressure at which the *i*th IC was working.

By grouping and rearranging terms in Eq. (3.3), the number of pions $N_\pi(Z_0)$ in the beam at Z_0 along the beam line can be expressed as

$$N_\pi(Z_0) = S_{i(\mathrm{cor})} M_i \ , \tag{3.4}$$

where

M_i = multiplier for the *i*th IC (pions per corrected count);

$S_{i(\mathrm{cor})}$ = number of corrected counts of the *i*th IC.

The last parameter can be expressed explicitly as

$$S_{i(\mathrm{cor})} = S_i \frac{(1-A_i)e^{-L_i/\lambda_\pi}}{\left[1+\sum_j G_j \langle R_j \rangle\right]} \frac{TP_{0i}}{T_0 P_i} \ , \tag{3.5}$$

where

$L_i = Z_i - Z_0$;

λ_π = pion decay length ($=\beta_\pi \gamma_\pi c \tau_\pi$);

A_i = fractional loss of pions due to scattering and absorption in matter along the pion path from Z_0 to Z_i.

D. Beam contamination

Protons, muons, and positrons are the three charged-particle species which contaminate the beam. The muons came mainly from two sources: (i) "cloud" muons (or "target" muons) from pion decays near the production target and (ii) decays of pions in the secondary beam channel downstream of the last bending magnet. Muons from pion decays in the channel between the first and last bend have very little chance of getting past the last bend and hence give a negligible contribution to the muon flux.

1. The proton contamination G_p

The proton contamination G_p had to be measured especially carefully because the high specific ionization of protons at the beam momentum affected the IC's disproportionately; also the contamination varied with time. G_p was determined by time-of-flight (TOF) measurements with the scintillation counters TB1 and TB2 over the path from the production target to the counters. The arrival times relative to pions of muons and protons in the TB1 and TB2 counters are −1.5 and 103.7 ns, respectively. Thus these TOF measurements were useful for differentiating protons from pions, but did not give good separation of muons from pions.

Practically, G_p was determined by using special machine pulses in which the H^+ primary beam was "chopped" to give a microstructure at 1 MHz (i.e., the 0.2-ns-wide micropulses were 1 μs apart instead of the normal 5 ns) and by scaling the numbers of protons (n_p) and pions (n_π) measured in a number (H_s) of micropulses. These special pulses were intermixed with normal running and the scalers n_p, n_π, and H_s were written on the data tapes at intervals.

For runs summarized on the first five summary tapes, G_p was about 4% and fluctuated by about 1%. Following a retuning of the beam, it was about 1.5% and fluctuated by only a fraction of 1%.

2. The muon contamination G_μ

The muon contamination G_μ from the decay of beam pions could not be measured experimentally, and depended on the geometry of the detector considered. A Monte Carlo program MUFLUX was written to simulate $\pi_{\mu 2}$ pion beam decays along the P^3 beam line to determine G_μ for each of the monitors. The starting point of the pion generation was the downstream end of the final bending magnet, and the effects of the upstream lead and magnetic collimators (see Fig. 1) and the lead collimator (Fig. 5) were included. G_μ was calculated for the thick IC, S_1 and S_2 counters, and TUIC. As in the collimator program MUSCAT, this code incorporated the Molière theory of multiple Coulomb scattering. The resulting values of G_μ for different device locations are summarized in Table II.

3. The cloud muon contamination $G_{\mu c}$

The cloud muons are formed by pions decaying between the production target and the first bending magnet. Muons that have the proper momentum and direction travel along the P^3 beam line. At 522 MeV/*c* it is not possible to differentiate the muons from the pions reliably with a TOF measurement, and so $G_{\mu c}$ was determined by extrapolating lower-momentum data. Several measurements of $G_{\mu c}$ were made at beam momenta of 400 and 450 MeV/*c* yielding (0.87±0.18)% and (0.69±0.06)%, respectively. The value of $G_{\mu c}$ at 522 MeV/*c* was calculated to be

$$G_{\mu c} = (0.5 \pm 0.1)\% \ ,$$

at the location of the S_1,S_2 telescope.

4. The positron contamination G_e

The positron contamination G_e was obtained from the work of Briscoe *et al.*,[16] who describe measurements in the LAMPF P^3 channel for both positive and negative beams of momenta 200 to 625 MeV/*c*. We use the value

$$G_e = (0.5 \pm 0.1)\% \ .$$

TABLE II. Muon contamination of the pion beam.

Device	G_μ (%)	$G_\mu \langle R_\mu \rangle$ (%)
Thick IC	10.22±0.10	10.39±0.10
S_1	10.18±0.10	10.18±0.10
S_2	10.12±0.10	10.12±0.10
TUIC	14.45±0.10	14.64±0.10

E. Corrections to the monitor counts

In the course of the experiment different parameters affecting the beam monitors varied (such as ambient temperature, pressure, beam contamination, beam intensity, etc.). Since the fluctuations were quite small and smooth with time, the corrections were made on each of the eight pion-beta-decay summary tapes (ST's), rather than on a single-run basis.

1. Corrections to the $\pi_{\mu 2}$ monitor counts

The dead-time correction (C_{DT}) depends on the beam intensity. This was calculated from the measured pulse lengths and counting rates. Figure 6(c) shows the correction C_{DT} (%) for the eight ST's. The values are typically 1.5%; for runs summarized on ST3 and ST4 lower and higher beam intensities were used, resulting in the observed variations of C_{DT}. The accidental-counts correction (C_{AC}) is calculated from single coincidence and delayed coincidence rates, to give $C_{\mathrm{AC}}=7\times10^{-5}$, at the average beam intensity.

The last correction C_{asy} (due to vertical motion of the beam) was determined by combining the results from the Monte Carlo program PIMUASY and the measured asymmetry $(T-B)/(T+B)$ during the experiment. The points in Fig. 6(a) show the variation of the detection solid angle of the $\pi_{\mu 2}$ monitor as a function of the beam asymmetry. The indicated uncertainties are statistical. The curve is a simple quadratic fit to the Monte Carlo results. C_{asy} was determined by considering the measured asymmetry when data were taken, the asymmetry when the $\pi_{\mu 2}$ monitor was calibrated, and the result of the fit. Figure 6(b) shows C_{asy} as a function of the eight pion-beta-decay ST's.

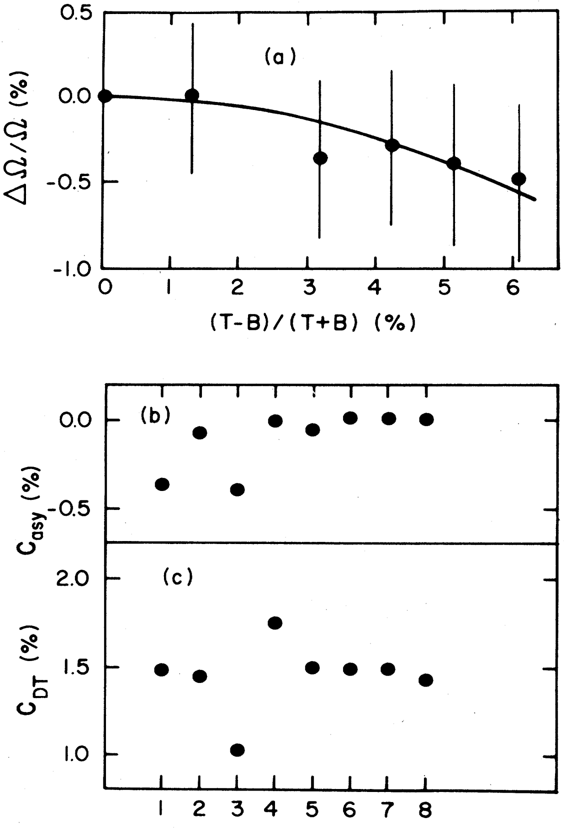

FIG. 6. Corrections to $\pi_{\mu 2}$ monitor counts by summary tape: (a) results of the simulation of the effect on the solid angle of vertical beam motion; (b) resulting corrections, by summary tape; (c) dead-time correction.

2. Corrections to the ionization-chamber counts

The corrections affecting the IC's are common to the thick IC and the TUIC with one exception: an offset was introduced on the TUIC electrometer output voltage to keep the Vidar VFC from automatically switching polarity on fluctuations near zero voltage. The offset correction reduced the raw TUIC counts by 2% to 5%.

The first common correction is due to temperature and pressure variations during the experiment. This correction was made separately for each run and did not exceed 2%.

The second correction is due to beam contamination, of which the most important (in terms of variation) is the proton contamination. The ionization loss of protons at the beam momentum is about 3 times that for pions, resulting in a 12% correction for early runs and a 4.5% correction for later ones. Muon and electron contaminations were assumed to be stable, at a total of 11% for the thick IC and 15% for TUIC, which was further downstream.

The third correction is the pion-decay term which accounts for the position of the IC's relative to the standard reference point Z_0. The correction was found to be 1.2627 and 1.3141 for the thick IC and TUIC, respectively.

The fourth and final correction is the term which takes into account scattering and absorption of pions in matter along the pion path from Z_0 to the IC position. The first part of this correction only concerns the TUIC and is due to the pion absorption in the two counters S_1 and S_2 (see Fig. 5). This absorption correction, which only applies to the last four ST's (because S_1 and S_2 were not in position earlier), was determined by placing plastic sheets of different thicknesses along the beam line and measuring the corresponding rates in the TUIC. The correction for S_1,S_2 was (1.013 ± 0.001). The other pion absorption and scattering corrections were calculated to be 0.27% for the thick IC and 0.44% for TUIC.

F. Calibration of the beam monitors

The procedure for determining the beam-monitor multipliers may be summarized as follows:

(a) Calibration of the beam monitor at low beam intensity by counting the beam rate with the pair of scintillation counters S_1,S_2.

(b) Correction, if necessary, of the calibration for the effects of temperature, pressure, beam contamination, etc.

(c) Extrapolation of the low-beam-intensity calibration to the higher beam intensity at which the data were taken.

1. *Calibration of the $\pi_{\mu 2}$ monitor*

Data on the ratio of $\pi_{\mu 2}$ counts to $S_1 S_2$ counts were taken at several (low) beam intensities and extrapolated to zero intensity. When the $S_1 S_2$ counts were corrected for beam contamination and the relative positions of the detectors, a multiplier of 4110±66 pions (at Z_0) per $\pi_{\mu 2}$ count was obtained. The error of 1.6% includes uncertainties in the straight-line fit, beam contamination (largest uncertainty), and absorption corrections.

2. *Calibration of the two ionization chambers*

The same technique of extrapolation to zero beam intensity was used for the ion chambers. The extrapolation to high beam intensity required calibration of the electrometers used, which was done using two Keithley model 261 pA current sources. In the case of the thick IC the calibration relied on the scaling and linearity of one current source as calibrated by a Keithley model 616 electrometer maintained by the standards group of LANL's E Division to a precision of better than 0.25%, while the calibration of the TUIC electrometer was extrapolated (using the other current source) by a step-by-step technique in which a current measured on one range was compared with the same current measured on another.

The final values for the multipliers were

$$(8.125 \pm 0.106) \times 10^5 \text{ pions/count for thick IC },$$

$$(1.983 \pm 0.022) \times 10^3 \text{ pions/count for TUIC }.$$

The errors of 1.3% and 1.1%, respectively, are due to uncertainties in the straight-line fit, absorption correction, and electrometer scaling factor.

G. Total number of pions in the beam

The number of pions in the beam at the standard reference point Z_0 for each pion-beta-decay ST was determined for the three beam monitors by multiplying (i) the raw monitor counts as read by the monitor scalers and written on the data tapes, (ii) the overall correction factor affecting the monitor, and (iii) the monitor multiplier.

Figure 7 shows the relative variation of the three monitors as a function of the ST. The calibration was done at the end of the series of runs and is represented by the point C on the figure. Although the monitors drift over the course of the experiment, it is by a maximum of 1% from the mean and there is no clear reason to prefer any of the three monitors; they are therefore all used.

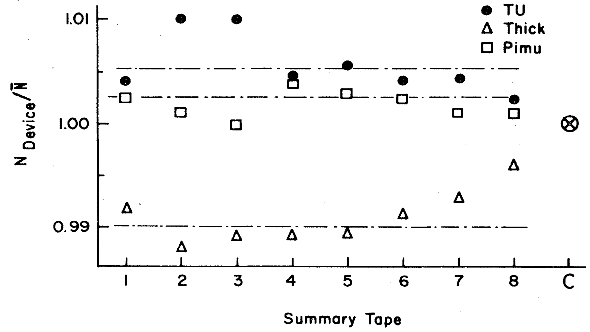

FIG. 7. Comparison of the three primary monitors, by summary tape. The point C is for the calibration runs, which were done at the end of the experiment.

The total number of pions in the beam at the standard reference point Z_0 was determined to be

$$N_\pi = (2.1498 \pm 0.0219) \times 10^{14} \text{ (pions) }. \qquad (3.6)$$

The uncertainty of 1.04% is the combination in quadrature of the uncertainties of the three beam monitors.

H. Beam momentum and phase space

To determine the pion-beam momentum p, measurements were made of the time of flight (with respect to a signal derived from the acceleration rf waveform, the T201 timing signal) of the six following particles: π, p, d, t, ${}^3_2\text{He}$, and ${}^4_2\text{He}$. This was done by mounting a scintillation counter along the beam line 7.6 cm downstream from the vacuum tank beam exit window and by analyzing the (two-dimensional) scatter plot of pulse height vs TOF. The pulse heights gave unambiguous particle identification. A least-squares fit to the differences in TOF gave a beam momentum of

$$p = 522.1 \pm 0.8 \text{ MeV}/c , \qquad (3.7)$$

which corresponds to a pion total energy of 540.4 MeV. This is in agreement with the value expected from magnetic-field measurements of the beam magnets. The momentum bite of the beam was taken from previous measurements and beam-transport calculations[11] to be

$$\Delta p/p = 5\% \text{ (FWHM)} \qquad (3.8)$$

(FWHM = full width at half maximum).

To measure the beam spatial characteristics (phase space), a set of three multiwire proportional chambers (MWPC's) was installed in the beam line, just downstream from the vacuum tank snout. The measurements were made with both a π^+ beam and a "pure" proton beam with similar defining apertures (jaw settings) and equivalent particle-separation degraders at the beam's intermediate focus.

The phase-space measurements (transverse spatial and angular coordinates) were fitted with Gaussian distributions and the standard deviations of the fits were calculated at the beam-waist position, 214 cm from the upstream end of the magnetic collimator, i.e., at about the center of the decay region. The results of the fits to the phase-space data are

$$\begin{aligned} \sigma_X &= 1.44 \pm 0.04 \text{ cm} , \\ \sigma_{X'} &= 3.93 \pm 0.13 \text{ mrad} , \\ \sigma_Y &= 0.84 \pm 0.10 \text{ cm} , \\ \sigma_{Y'} &= 5.28 \pm 0.35 \text{ mrad} , \end{aligned} \qquad (3.9)$$

where

$\sigma_{X,Y}$ = standard deviation of the X,Y transverse spatial coordinate at the waist;

$\sigma_{X',Y'}$ = standard deviation of the X,Y angular beam divergence at the waist.

These parameters were used in the calculation of acceptance described in Sec. VI C.

IV. CALIBRATION RUNS

Besides $\pi\beta$ data taking we also took calibration data with a 1.3-cm-thick CH_2 target near the center of the decay region with π^+ and π^- beams, and with a π^- beam and hydrogen gas at atmospheric pressure filling the tank. The π^0's produced by charge exchange in these runs were used to calibrate the energy scale, conversion efficiency, and absolute timing of the detectors. By subtracting the π^+CH_2 spectrum from the π^-CH_2 spectrum we obtained energy response curves for the nearly monoenergetic π^0's from the π^-p reaction, which showed the long tail to low-apparent-measured energies usual for total absorption γ detectors.

A. Energy calibration

The γ detectors were initially calibrated with a 270 MeV/c electron beam, to give initial values of the factors relating pulse heights to total energy for each total absorption block and each converter slab. Runs at 180 and 360 MeV/c verified the linearity of pulse height with electron energy. The final calibration was then done using π^-CH_2 runs. The total energy is found from a weighted sum of the pulse heights from the converters, the scintillators, and the lead-glass blocks:

$$E = w_C P_C + w_S P_S + w_B P_B \ ,$$

where P_C, P_S, and P_B are the total normalized pulse heights from the converters, scintillators, and blocks, respectively, and w_C, w_S, and w_B are the weights for these three quantities.

The π^-CH_2 runs were used to determine the ratios of the weights so that total measured energy was independent of the conversion plane, and so that the best resolution was obtained. The scaling of the weights was done so that the central value of a Gaussian distribution fitted to the part of the spectrum between 400 and 700 MeV matched (within 1 MeV) the expected mean value predicted from Monte Carlo calculations. Since the actual energy scale is not important to the final result, this was felt to be an adequate procedure, and consistent with the way in which measured energies were used in the analysis. Figure 8 shows the energy spectrum from a π^-CH_2 run; fitting the peak with a Gaussian gives a central value for the energy of 529 MeV (and a width of 16%), slightly below the mean value 536 MeV for $\pi^-p \rightarrow \pi^0 n$ as predicted by a Monte Carlo calculation using our beam parameters and measured angular distributions.[17] The π^-CH_2 spectrum includes π^-C charge-exchange (CEX) events; the π^-p spectrum can be found by subtracting an appropriately normalized π^+CH_2 spectrum, assuming that the reaction $\pi^-C \rightarrow \pi^0 + X$ has the same cross section as $\pi^+C \rightarrow \pi^0 + X'$. A typical π^+CH_2 energy spectrum is shown in Fig. 9; a Gaussian fit has a central value for the energy of 509 MeV and a width of 19%. The corrected spectrum has a central energy in agreement with the Monte Carlo mean value. Figure 10 shows the three spectra.

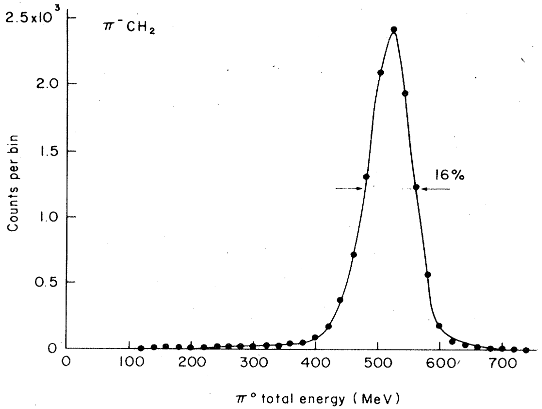

FIG. 8. Total-energy spectrum from a π^-CH_2 run.

B. Energy-response function of the detector

Total absorption γ detectors typically have a skew pulse-height response to a monoenergetic beam, with a long tail extending to low pulse heights. We assumed that the corrected spectrum shown in Fig. 10 is the energy-response function for our detector at the low-beam intensities used for calibration. A typical pion-beta-decay run was at several times the beam intensity for π^+CH_2 data, and there was a significant amount of random pulse height in the detectors. Figure 11(a) shows the spectrum from a special run in which event-read-out cycles were triggered by a free-running pulse generator ("clock" trigger). This had a mean energy and width of (17.8 ± 17.3) MeV. Figure 11(b) shows the result of folding curve C of Fig. 10 with the curve of Fig. 11(a). The resulting curve has, between 400 and 800 MeV, a mean energy of 556 MeV, and a standard deviation of 43 MeV. From this, the expected apparent mean energy of pion-beta-decay events (which we expect to have a mean energy of 523 MeV) would be $556 - 536 + 523 = 543$ MeV with a width of 43 MeV, which is what we found. It was assumed that the response to pion-beta-decay events would have the shape of the curve of Fig. 11(b) shifted down by 13 MeV (because the data was binned, it was easier to make this small shift, rather than to scale the curve).

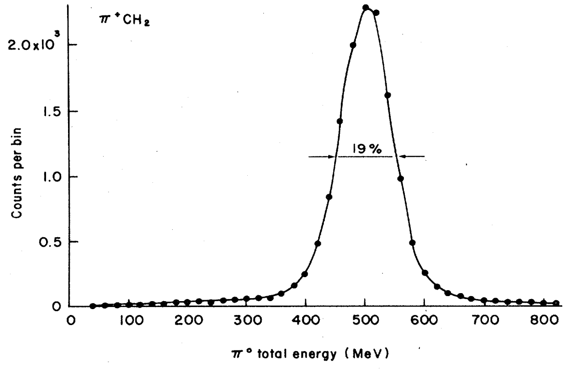

FIG. 9. Total-energy spectrum from a π^+CH_2 run.

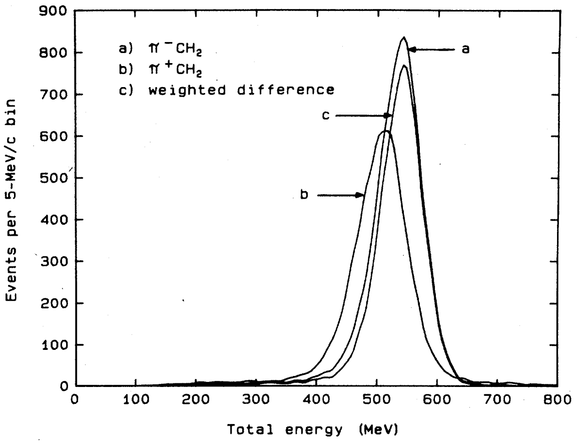

FIG. 10. Total-energy spectra from π^+ and π^-CH_2, with weighted difference.

C. Timing calibration

The LAMPF primary proton beam is time-structured with a period of 5 ns because the accelerating waveform in the early stages has a frequency of 201 MHz. Because of the isochronicity of the beam line, the pions arrived in the decay region in bunches 5 ns apart, with a width of about 250 ps. By measuring the times of the γ rays relative to a signal (T201) derived from the rf signal, a factor of 2 improvement in discrimination against background was obtained as compared with using just the time difference between the γ rays. The electronics which selected a T201 pulse to be fed to the CAMAC time-to-digital converter (TDC) was designed to be close to 100% efficient and hence occasionally produced ambiguities of ±5 ns. The ambiguities were resolved, and corrections for changes in the transit time of the signal from accelerator to our electronics were made, by software using a set of constants for each distinct set of runs. Basically, after correcting for changes in the cable and amplifier system, the smallest time from the T201 signal to the mean of the two γ times, modulo 5 ns, was chosen. The time distributions had a standard deviation of approximately 250 ps (FWHM of 580 ps), as shown in Fig. 12. The resolutions of the two arms of the detector differed slightly, the standard deviations of the T_1, T_2 timing distributions being for a single run

$$\sigma_{T_1}=248\pm4 \text{ ps}, \quad \sigma_{T_2}=258\pm8 \text{ ps} . \tag{4.1}$$

Time shifts and drifts of the rf signal and of the individual counters during the experiment were corrected by analyzing π^+CH_2 data, which were taken at regular intervals during the experiment (one π^+CH_2 run for each pion-beta-decay run). During analysis the data from the π^+CH_2 runs were used to update all timing corrections for the corresponding pion-beta-decay run. Run-to-run shifts were small, typically less than 50 ps; the final overall time resolutions for the entire run were

$$\sigma_{T_1}=267\pm6 \text{ ps}, \quad \sigma_{T_2}=274\pm10 \text{ ps} . \tag{4.2}$$

D. Conversion probability of the γ rays in the detectors

The conversion probability P is the probability for a γ ray incident on the forecrate (i.e., the converter slab and scintillator array shown in Fig. 3) within the fiducial area, to convert and to be detected by the scintillator planes; P was determined by analyzing the π^-CH_2 and the π^-H_2 data. The model used to determine P is somewhat different for the two kinds of data.

As shown in Fig. 3, the γ-detector forecrate was composed of three sections (each section consisted of a converter plane, an X scintillator plane, and a Y scintillator plane) with veto counters placed in the front (and to the

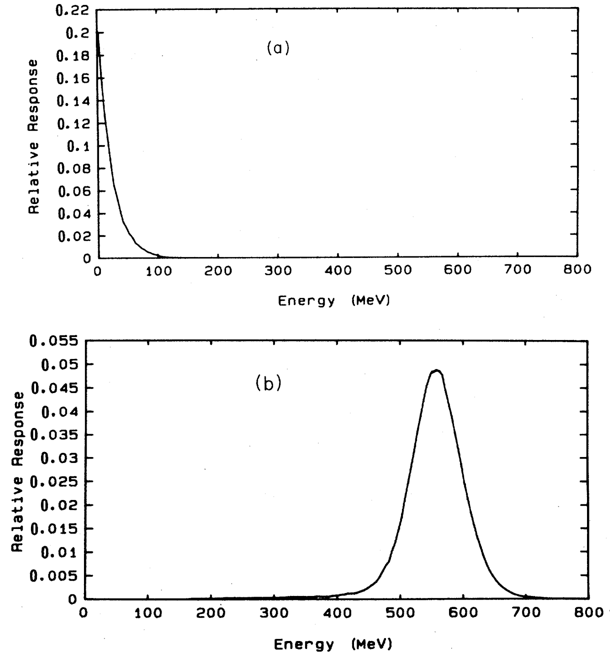

FIG. 11. Energy response of detector: (a) total energy with clock trigger; (b) expected response function for π^-p at high-date rates (see text).

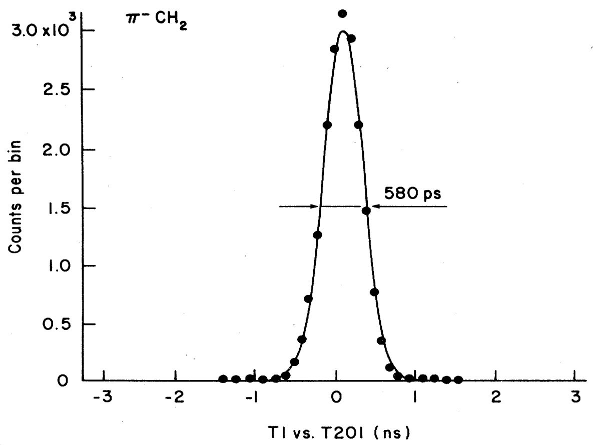

FIG. 12. Timing distribution from π^-CH_2 uncut data. Plotted along the abscissa is the time difference between the time in arm 1 (T_1) and a signal derived from the machine rf (T201).

TABLE III. Solid angles subtended by the sections at the CH_2 target.

Section	Solid angle (sr)[a] Arm 1	Arm 2	R_{ij}[a] Arm 1	Arm 2
1	4.0146×10^{-2}	4.0543×10^{-2}	1.1392	1.1455
2	3.7553×10^{-2}	3.7884×10^{-2}	1.0656	1.0704
3	3.5241×10^{-2}	3.5392×10^{-2}	1.0	1.0 (def)

[a] Uncertainty on the solid angles is 0.1%, on the ratios 0.15%.

side) of the forecrate. The thicknesses of sections 2 and 3 were identical, whereas the thickness for γ conversion of section 1 was smaller by that of one scintillator (because the Y counters of planes 1 and 2 act as part of the converter for planes 2 and 3).

The ratio a is defined as

$$a=\frac{\text{conversion probability section 1}}{\text{conversion probability section 2 or 3}}\ .$$

Using tabulated values of radiation lengths,[9]

$$a=0.961\pm0.004\ .$$

The data were then fitted with the following model:

$$N_1=CR_{13}Ea\ ,$$

$$N_2=CR_{23}E(1-Ea)\ ,$$

$$N_3=CR_{33}E(1-E)(1-Ea)\ ,$$

and

$$P_1=N_1/CR_{13}\ ,$$

$$P_2=N_2/CR_{23}\ ,$$

$$P_3=N_3/CR_{33}\ ,$$

where

N_i = number of detected events in section i ($i=1,2,3$);

C = overall normalization constant;

E = conversion probability for a γ ray reaching section 2 or 3;

$R_{ij}=\Omega_i/\Omega_j$;

Ω_i = solid angle of section i;

P_i = probability of a conversion occurring in section i.

The total conversion probability P is $(P_1+P_2+P_3)$. The ratios P_i/P were used in the Monte Carlo program PIOBETA, which calculated the acceptance of the detector; the value of P is then used to normalize the results.

The π^-CH_2 data have two nice features. First, they have good statistics, which permit an accurate determination of the fitted parameters. Second, after selecting only events in which the outer scintillators in the conversion plane (the guard ring) do *not* fire, the π^0 energy spectrum is very clean, as shown in Fig. 8. Thus the data represent π^0's produced by charge exchanges $\pi^-p\rightarrow\pi^0n$.

On the other hand, the data have two inconvenient aspects. The constant C introduced in the model must be determined in addition to E, so a two-parameter fit is involved. Also, the relative solid angles R_{ij} of sections 1, 2, and 3 with respect to the polyethylene CH_2 target, are needed. These solid angles are calculated from the precise measurements made during the survey of the experiment and are given in Table III (the uncertainties in the solid angles are typically 0.15%).

The results (averages from all the π^-CH_2 data) are summarized in Table IV. Note the agreement between the two arms of the π^0 spectrometer. Averaging the two results and taking into account the uncertainties in the R_{ij}'s, we find

$$E=0.3497\pm0.0035\ ,$$

$$P=0.7195\pm0.0042\ .$$

For the π^-H_2 data, the forecrate was removed from the trigger of one of the γ detectors. The data corresponded to a signal in the lead-glass elements (converters or blocks), no veto, and a normal trigger in the other γ detectors. The γ conversion could take place in sections 1, 2, and 3, or in the rearcrate (the total-energy-absorbing lead-glass blocks). These data have two nice features. First, the constant C is no longer a free parameter since the following relation is satisfied:

$$C=N_1+N_2+N_3+N_b\ ,$$

where N_b is the number of events with signals only in the blocks.

Thus, there is only one free parameter (E) to be fitted. Second, only events with substantial pulse height in the three central blocks were accepted in this analysis. Consequently, all the R_{ij}'s are equal to one, which reduces the uncertainties in the determination of E.

On the other hand, the data have two inconvenient aspects. As seen in Fig. 13, the π^0 energy spectrum is contaminated by the presence of π^0's produced in the pion-production reactions $\pi^-p\rightarrow\pi^0\pi^0n$ and $\pi^-p\rightarrow\pi^-\pi^0p$. This meant that a severe cut on the total energy had to be made in order to select the π^0's produced by charge ex-

TABLE IV. Experimental results for the conversion probabilities.

Data	Conversion probability E Arm 1	Arm 2	Total conversion probability P Arm 1	Arm 2
π^-CH_2	0.3498 ± 0.0041	0.3495 ± 0.0042	0.7198 ± 0.0052	0.7191 ± 0.0053
π^-H_2	0.3484 ± 0.0092	0.3413 ± 0.0085	0.7180 ± 0.0116	0.7086 ± 0.0111

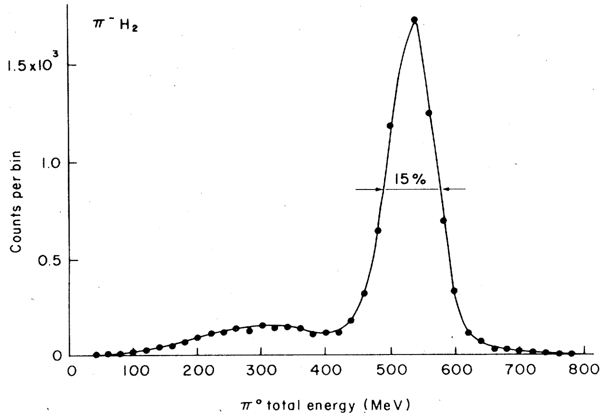

FIG. 13. Total energy spectrum from a $\pi^- H_2$ run.

change. Also, as a consequence of these cuts, the interesting data have poorer statistics, and this increases the uncertainty of the determination of E. The averaged experimental results for the $\pi^- H_2$ data are summarized in Table IV. Again, very good agreement is observed between the two γ detectors. Averaging the results of the two arms, one finds

$$E = 0.3446 \pm 0.0062 \; ,$$

$$P = 0.7131 \pm 0.0080 \; .$$

The final values for E and P were obtained as follows. The result E determined from the $\pi^- H_2$ data analysis needs to be corrected slightly since, on the average, the γ rays incident on the forecrate, which are produced in the gaseous hydrogen target, are not perfectly normal to the sections. According to a Monte Carlo program calculation (PIONEUT) the correction is $\langle \cos\theta \rangle = 0.9926$, where θ is the angle between the normal to the forecrate and the incident γ ray. The uncertainty (rms) in E is increased by half of this correction and by the estimated effect of the contamination of the π^0's.

The modified experimental results E are given by

$$\pi^- CH_2{:}\; E = 0.3497 \pm 0.0035 \; ,$$

$$\pi^- H_2{:}\; E = 0.3420 \pm 0.0063 \; .$$

The final value $\langle E \rangle$ is obtained by making an average, weighted by the errors, of the two results:

$$\langle E \rangle = 0.3483 \pm 0.0044 \; . \tag{4.3}$$

The combined probability for a normally incident γ to convert in one γ detector within the fiducial area is then

$$P(\langle E \rangle) = 0.7174 \pm 0.0043 \; . \tag{4.4}$$

The experimental result $P(\langle E \rangle)$ can be compared with a Monte Carlo prediction. Reference 18 gives a semiempirical expression for the conversion probability E as a function of the γ energy in 0.68 r.l. of LF5 lead glass:

$$E_c = 0.33 + 0.1 \log_{10}(0.01\, E_\gamma) \; ,$$

where E_γ = incident γ energy in MeV. In our case, the mean energy $E_\gamma = 270$ MeV, and the thickness of section 2 or 3 is 0.6187 r.l. Assuming that E_c varies linearly with the material thickness, we calculate

$$\begin{aligned} E_c &= 0.3395 \; , \\ P(E_c) &= 0.7061 \; . \end{aligned} \tag{4.5}$$

The result (4.5) is in good agreement (1.6%) with the experimental result (4.4) above.

The value of P above is for the energy distribution of γ rays as seen in the calibration runs; for pion-beta-decay data the energy and angle distributions are again slightly different (e.g., more tendency to equal energy for the two γ's), so a small upwards correction gives a joint conversion efficiency of

$$P^2 = 0.5151 \pm 0.0062 \; . \tag{4.6}$$

The overall uncertainty is due to statistical uncertainties, and uncertainties in geometry, material thicknesses, and pion production.

V. BACKGROUNDS

Background events arise in several ways: two-particle decays of beam particles, two-particle events from interactions in the material of the apparatus, and spurious coincidences between single-particle events. Neutron-induced reactions are assumed to be of the single-particle type. The most important background is from the structure-dependent part of the radiative decay $\pi^+ \to e^+ + \nu + \gamma$. This background was underestimated in the previous analysis.[1]

A. Two-particle process

Table V lists real two-particle processes with estimates of their probability. The yield per incident pion is the geometrical yield as calculated by Monte Carlo simulation. The value for the process $\pi \to e\nu\gamma$ is calculated using only the structure-dependent parts;[19,20] using either value of the structure-dependent parameter γ found in Ref. 20 ($\gamma = 0.44$ or -2.36) gives the same result. The value for the process $\mu \to e\nu\nu\gamma$ is the inner-bremsstrahlung rate[21] assuming all the muons come from π^+ decays in flight. The π^+ CEX rate is an upper limit

TABLE V. Two-particle processes.

Process	Yield/Incident π	After cuts	Neutral-trigger yield
$\pi^+ \to \pi^0 e^+ \nu$	1.68×10^{-11}	1.6×10^{-11}	0.84×10^{-11}
$\pi^+ \to e^+ \nu\gamma$	5.9×10^{-11}	1.61×10^{-11}	$(0.81\pm0.45)\times10^{-13}$
$\mu^+ \to e^+ \nu\nu\gamma$		$<7\times10^{-15}$	$<5\times10^{-17}$
π^+ CEX on gas	$<1.1\times10^{-16}$	$<1.1\times10^{-16}$	$\sim5.5\times10^{-17}$

on the production of π^0 by charge exchange made assuming that the residual gas is nitrogen and using a cross section estimated from the π^+CH_2 data. The cuts applied are cuts on the variables D and C (described below), which essentially measured the transverse momentum of the two detected particles, and a cut on their total energy E.

The cuts are designed to have no effect (in principle) on the pion-beta-decay detection efficiency; they reduce other processes significantly. For pion-beta-decay and CEX events the "neutral-trigger yield" is calculated using a conversion efficiency P^2 of 0.52. For the $\pi\rightarrow e\nu\gamma$ and $\mu\rightarrow e\nu\nu\gamma$ events, a single γ efficiency of 0.72 and a charged-particle veto inefficiency of $(0.7\pm0.4)\%$ give an estimated neutral-trigger efficiency of $(5.0\pm2.8)\times10^{-3}$. The veto inefficiency was estimated in two ways: from measurements of the variation of efficiency as a function of counter high voltage using charged particles $[(1.1\pm0.5)\%]$, and from the pulse-height spectra obtained using charge-integrating analog-to-digital converters (ADC's) $[(0.3\pm0.3)\%]$. These are combined to give an estimate of $(0.7\pm0.4)\%$ where the error is systematic. Thus the rate for $\pi\rightarrow e\nu\gamma$ being misidentified as pion beta decay is estimated to be $(0.94\pm0.54)\%$ of the pion beta decay, giving a correction factor of (0.9907 ± 0.0054) to the number of observed events.

B. One-particle processes

The rate for single-particle neutral counts in either arm is observed to be 5×10^{-6} per incident pion; this is believed to come primarily from interactions of beam pions in the collimator or tank. Other processes, such as $\pi\rightarrow\mu\nu\gamma$, contribute about 20% of this rate. The energy spectrum of these neutral counts falls off greatly at high measured energy.

The double-coincidence raw trigger rate of $0.54\ s^{-1}$ was consistent with this single-particle rate giving random coincidences of uncorrelated counts within the trigger-resolving time. This random background, after time and kinematical cuts, was about 1% of the pion-beta-decay rate, and was subtracted as described in Sec. VI E.

VI. ANALYSIS

A. Summary tapes

The analysis proceeded in several stages: the first reduced the data sample to the set of summary tapes (ST's). The times of conversion of each γ ray (T_1,T_2) relative to the T201 signal was computed and a χ^2 statistic formed:

$$\chi_T{}^2=\frac{T_1{}^2}{\sigma_1{}^2}+\frac{T_2{}^2}{\sigma_2{}^2}\ . \tag{6.1}$$

The total energy E was also found from the pulse heights in the converters, blocks, and scintillators. An energy cut $E\geq190$ MeV and a time cut of $\chi_T{}^2\leq18$ were sufficient to reduce the data sample to 11 700 events (primarily by the time cut). A small proportion of pion-beta-decay events was also rejected in this process due to the algorithm for calculating the times; this led to corrections described below. When making the ST's, the appropriate π^+CH_2 run was replayed first to update the timing constants and to use the source data to update the calculated gains of the lead-glass element PM's. The ST's then contained records of events which satisfied the software cuts, with the scintillator data time-corrected, records of the relative gains of the lead-glass element PM's, and scaler information. These ST's were then further reduced by using cuts at $E\geq225$ MeV and $\chi_T{}^2\leq13.5$ to a sample of 7000 events on summary ST's (SST's).

Note that we have frequently used more significant figures in quoting numbers in this paper than is apparently justified; this is to minimize errors introduced by early rounding.

B. Final event selection

To select the final pion-beta-decay sample we cut on three variables: (a) $\chi_T{}^2$, described above, (b) D, a coplanarity parameter measuring the distance of the line joining the points of conversion from the beam-center line, as shown in Fig. 14, and (c) C, a momentum-conservation parameter which is a measure of the deviation from equality of the transverse momentum of the two photons:

$$C=100\ln\left|\frac{E_1R_1}{E_2R_2}\right|\ ,$$

where E_1,E_2 and R_1,R_2 are the measured energies of the γ's and the distances of their points of conversion from the beam.

1. Timing cut and its efficiency

Pion-beta-decay timing distributions, due to the decays occurring throughout the decay region, were generated using the Monte Carlo program PIOBETA. The rms width of the timing distribution obtained by the Monte Carlo program was $\sigma_T=71$ ps for both detectors. This value was folded with the two point-source rms widths, as measured using π^+CH_2 data, to simulate the real pion-beta-decay rms widths of the timing distributions in the experimental apparatus.

Figure 15 shows two distributions of the time T_1 for

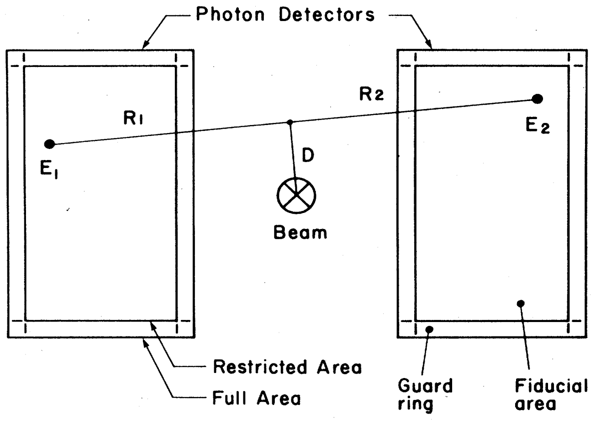

FIG. 14. Diagram of photon detectors, showing definition of parameters used in the analysis.

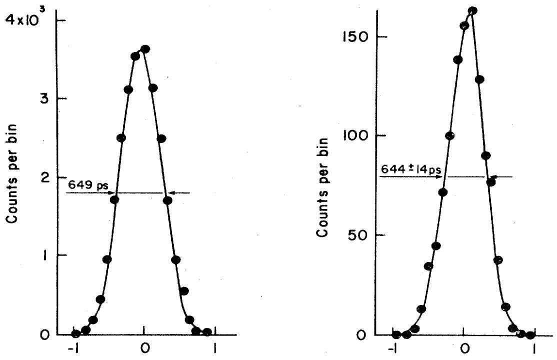

(a) Monte Carlo TIS (ns) (b) T1 vs. T201 (ns)

FIG. 15. Timing distribution for pion-beta-decay events: (a) as generated by Monte Carlo PIOBETA; (b) for class A events after all cuts.

one arm. One was obtained with the Monte Carlo program and the other from the pion-beta-decay data analysis (events with energy greater than 400 MeV). Note the good agreement of the shape and width of the two distributions.

The distributions of the times measured with calibration data were closely normal, so we expect $\chi_T{}^2$ to be distributed according to the χ^2 distribution for two degrees of freedom. The final cut of $\chi_T{}^2 \leq 10$ then has an efficiency

$$E_T = 0.9892 \pm 0.0073 \,, \qquad (6.2)$$

where the error represents our uncertainty as to how precisely the times are normally distributed and uncorrelated and how well the widths are known.

2. *D cut and its efficiency*

As shown in Fig. 14, the coplanarity parameter D defines the coplanarity of the detected γ rays with the incident beam. The kinematics of the pion-beta-decay process requires the coplanarity parameter to be small, whereas background events may have a large value of D. The expected distribution of D for the pion-beta-decay events was generated by the Monte Carlo program PIOBETA, in which the parameter D was computed the same way as in the off-line software analysis. Figure 16(a) shows the D distribution obtained with the Monte Carlo program, while Fig. 16(b) shows the distribution of energy-selected events from the pion-beta-decay data analysis. The irregularity of both curves arises from the granularity of the detectors.

To avoid a large uncertainty in the efficiency of this cut, it was made at $|D| = 75$ mm, giving

$$E_D = 0.9995 \pm 0.0005 \,, \qquad (6.3)$$

where the uncertainty is primarily systematic. This cut reduced background by a factor of about 3, at all energies.

3. *C cut and its efficiency*

The expected C distribution was Monte Carlo generated; Fig. 17(a) shows the generated distribution while Fig. 17(b) is that for energy-selected events from the pion-beta-decay analysis. The final cut was made at $|C| = 25$ giving

$$E_C = 0.9993 \pm 0.0005 \,, \qquad (6.4)$$

where again the uncertainty is primarily systematic. This cut varied in efficiency with energy, being most efficient in rejecting background at high total energy, unlike the $\chi_T{}^2$ and D cuts which reduced the background approximately equally at all energies. This was used to generate a high-statistics background spectrum as described below.

Finally, the total efficiency of the three off-line software cuts made on the data was

$$F_4 = E_T E_D E_C = 0.9880 \pm 0.0073 \,. \qquad (6.5)$$

The uncertainty is partly statistical and partly due to experimental uncertainties in the timing rms widths, the geometry of the detectors, the beam phase space, and the beam steering.

C. Monte Carlo program and acceptance

The acceptance of the apparatus was determined by the Monte Carlo program PIOBETA, which simulated the beam momentum spectrum, the measured beam phase space, the surveyed geometry of each detector, and the pion-beta-decay process using standard electroweak theory.

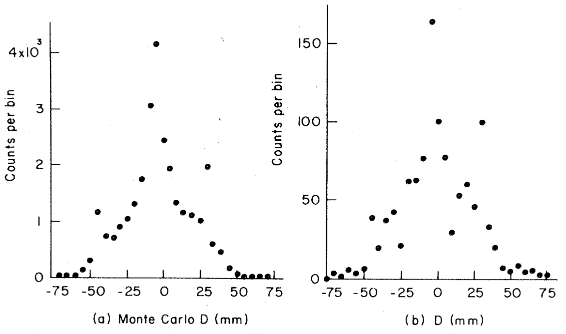

(a) Monte Carlo D (mm) (b) D (mm)

FIG. 16. Distributions of the parameter D for pion-beta-decay events: (a) as generated by PIOBETA; (b) for class A events after all cuts.

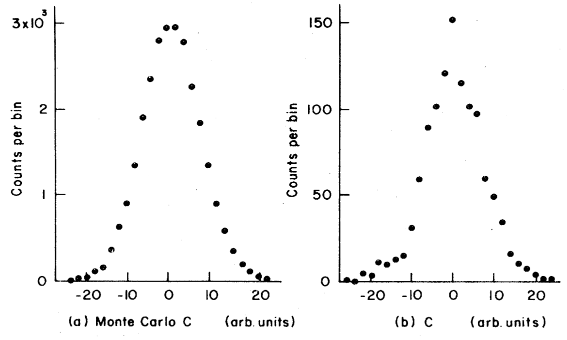

(a) Monte Carlo C (arb. units) (b) C (arb. units)

FIG. 17. Distributions of the momentum-conservation parameter C (see text for units): (a) as generated by PIOBETA; (b) for class A events after all cuts.

The program had a twofold purpose: (a) to determine the primary physical quantities needed to calculate the experimental pion-beta-decay rate (detection solid angle, self-veto correction, electron counter solid angle), and (b) to generate the distributions of physical parameters to determine cut efficiencies (π^0 total energy, $\chi_T{}^2$, D, etc.).

The apparatus and geometry considered in the program are as follows:

(i) The two γ detectors consist of a forecrate and a rearcrate (see Fig. 3). The forecrate is composed of three rectangular sections and of two veto counters, and the rearcrate of an array of fifteen lead-glass blocks.

(ii) Each section is defined by the intersection of four straight lines representing the scintillator edges of the fiducial area (see Fig. 14). The X and Y scintillators of the fiducial area and the lead-glass blocks are defined by their center and edges.

(iii) The frame of the vacuum-tank window is defined relative to the γ detector and to the two veto counters.

(iv) The electron counters are defined by two rectangular areas, one placed above and one below the beam line.

The main steps in the program are as follows:

(1) A pion is generated with the measured beam phase space (see Sec. III H).

(2) The pion-decay point along the beam line (Z axis) is chosen with a probability $(\beta\gamma ct_\pi)^{-1}$, from $Z_0=58$ to 240 cm, and the decay is chosen according to the kinematics of the beta-decay mode with use of the standard weak-interaction theory, and t_π is the pion lifetime.

(3) The two γ rays are traced into the γ detectors, where both are converted. The two sections i and j of the detectors where the conversions occur are determined and the points of intersection of the γ's with the two planes defining the sections i and j are calculated. Each section i of the forecrate is assigned a relative conversion probability determined from the data analysis (see Sec. IV D).

(4) An event is classified as good if the two γ's are within the fiducial-area limits. In this case, the program follows the electron and determines if it hits either one of the electron counters or one of the four vetoes.

(5) The measured γ energies are smeared, assuming that the γ energy resolution was $\sigma=1.53\sqrt{E}$ (σ and E in MeV), where the proportionality constant was determined from analysis of the $\pi^-\mathrm{CH}_2$ data. The quantities C, D, the times of conversion, and the sum of the two γ energies are computed.

(6) Selection criteria are applied to the event, and it is added to corresponding histograms.

(7) The program then returns to step (1) above, until sufficient events have been generated.

The overall acceptance for the two γ's to hit the detectors was found to be

$$\Omega=(\beta\gamma ct_\pi)^{-1}\int\eta(z)dz=(1.6200\pm0.0098)\times10^{-3} \quad (6.6)$$

per pion entering the decay region and undergoing a beta decay. The error is primarily from the statistics of the Monte Carlo program. This has to be corrected by a factor for vertical beam motions during the run as measured by the asymmetry of the $\pi_{\mu2}$ monitors, the factor being (0.9984±0.0004).

In addition, the event will be vetoed if the positron hits a veto counter, which occurs for an estimated (16.06±0.52)% of the events. The error is both from Monte Carlo statistics and from our estimate of the efficiency of the veto on low-energy positrons, or positrons which pass through the frame of the tank window.

The quantity T defined in Eq. (2.2) is

$$T=(3.534\pm0.031)\times10^{-11}\ \mathrm{s}\ . \quad (6.7)$$

Note, as mentioned earlier in Sec. II, that T depends only weakly on beam momentum: to a first approximation, T remains unchanged for a momentum variation (the length of the decay region and hence Ω increases with γ of the beam pion, while the proper time per unit path length decreases, so that the product does not change).

D. Correction factors

1. *Data-acquisition live time*

Since the beam monitors were recorded continuously, even during event readout cycles when no new events were accepted, the number of beam pions had to be corrected for the data-acquisition live-time fraction, which was 0.9973±0.0001, to give an effective number of pions

$$N_\pi=(2.1440\pm0.0218)\times10^{14}\ . \quad (6.8)$$

2. *Dalitz decays and early conversions*

Dalitz decays ($\pi^0\rightarrow\gamma e^+e^-$) and conversions in the tank window and veto counter, where the pulse height is sufficient to trigger the veto, will cause pion-beta-decay events to be lost. This factor was estimated in two ways: by calculation and by using $\pi^-\mathrm{CH}_2$ and $\pi^-\mathrm{H}_2$ runs with the veto counters out of the trigger. The data from the special runs were analyzed to select good π^0 events, and the fraction of such events with an in-time veto counter pulse was found. Table VI lists the results. Note that the CH_2 target causes some conversions as does the H_2 gas.

There is evidence in the analysis of the experimental data that the sample of π^0's was not pure, so we adopt for the probability of an early conversion or Dalitz decay on one side the value (0.0289±0.0026), which is the weighted mean of the theoretical and measured values for $\pi^-\mathrm{H}_2$ corrected for conversion in the gas. The correction for two-γ events is then

$$F_1=0.9430\pm0.0050\ . \quad (6.9)$$

3. *Trigger inefficiencies*

Three effects contributed to trigger inefficiencies: the timing spread of the logic signals at the left-right coin-

TABLE VI. Dalitz decays and early conversion probabilities.

Data	Calculated value[a]	Measured value
$\pi^-\mathrm{H}_2$	0.0281±0.0016	0.0340±0.0030
$\pi^-\mathrm{CH}_2$	0.0369±0.0020	0.0500±0.0035
Vacuum	0.0277±0.0016	

[a] Dalitz decays are 0.0058 per γ ray.

TABLE VII. Number of events by class.

Class	No. of events	Background	Net No. of events	Energy cut	Side veto correction
A	1144±33.8	13 ±2.2	1131 ±33.9	0.9737±0.0026	0.9923±0.0010
B and C	114±10.7	3 ±0.8	111 ±10.7	0.889 ±0.020	0.99 ±0.01
D	1± 1	0.4±0.2	0.6± 1.0	0.84 ±0.08	0.98 ±0.02

cidence circuit, dead time generated in the discriminators (which were fed with the summed pulse from the lead-glass on each side), and the dead time generated by the veto counters.

The first effect was estimated from measurements of the coincidence counter rate as a function of relative delay of the arm 1 and arm 2 signals (see Fig. 4), with a π^- beam and H_2 gas in the tank. The effect was small: 0.9970±0.0025.

The dead time of the constant-fraction discriminators used for the summed lead-glass pulses depended on the input pulse height. A conceptual model of the discriminator's mode of operation and of the input pulse-height spectrum was used to calculate a correction of 0.996±0.004. The distribution of the time of firing relative to the scintillator time of each of these two discriminators agreed with the model.

The last correction is larger; it also interacts with the previous one since charged particles will be vetoed and will not contribute to the "lead-glass" dead time. The veto dead time could not be precisely estimated if the hardware dead time alone was used, since it was not well known enough. A cut was made in the analysis rejecting events from the sample if the recorded time of a veto counter pulse was within an interval chosen to be wider than the hardware width. The veto dead time is then the width of this cut times the singles rate as measured outside this region; the value is (0.898±0.008).

Combining these three corrections gives

$$F_2 = 0.8917 \pm 0.0090 \ . \qquad (6.10)$$

There is another veto correction, due to showers leaking out to the side veto counters. The correction for this depends somewhat on the type of event and is given in Table VII.

4. *Software corrections*

Accidental counts in the scintillators could cause an event to be lost through computation of a bad χ_T^2 or by misclassifying the event. This primarily occurred in the process of making ST's, where a time window of 39 ns was used to select valid scintillator times for χ_T^2 calculation. Thus an accidental count within this range, on top of a real count, could lead to rejection of the event from the ST's. For the final sample, narrower time windows could be used, thus rejecting most accidental counts. Study of raw data runs gave an estimated loss of (4.1±0.3)% of the events, due to accidental counts (where the error is statistical). The model of accidental counts used predicted that (2.8±0.3)% of the surviving events would have an accidental count that did not result in rejection in the first pass, and indeed 2.8% (173/6171) such events were found.

There is an additional correction of 0.1% due to the 5 ns ambiguity in determining the times used for calculating χ_T^2 (see Sec. IV C).

We therefore have an overall software correction of

$$F_3 = 0.9581 \pm 0.0050 \ , \qquad (6.11)$$

where the error is increased because of systematic uncertainties.

E. Number of pion-beta-decay events and background subtraction

To estimate N_β we divided the events into classes according to whether they registered only in the fiducial area or also in the guard ring. Class A events had all the *XY* coincidence pairs inside the fiducial area; class B and C events were those with an *XY* coincidence also in the guard ring of arm 1 and arm 2, respectively; while class D events had guard-ring hits and fiducial-area hits on both sides. Table VII lists the numbers of events passing final cuts as described above, along with corrections which vary by class. A Monte Carlo calculation, including estimates of the effect of gaps between scintillators and the effect of a single electron traversing two adjacent scintillators, gave the weights for the classes shown in Table VIII. The weight is defined as the fraction of events of the given class which result from γ's directed into the fiducial area. Table VIII also gives the random background, the subtracted numbers of events in each class corrected for the class-dependent effects, the expected and observed ratios in each class, and the final number of events. The agreement between the expected and observed ratios for classes

TABLE VIII. Weights and ratios of events by class.

Class	Corrected No. of events	Weight	Expected ratio	Observed ratio	Weighted No. of events
A	1170.6±35.2	0.9983±0.0019	1.0 (def)	1.0 (def)	1168.6±35.2
B and C	126.2±12.5	0.528 ±0.021	0.101±0.004	0.108±0.011	66.6± 6.7
D	0.7± 1.2	0.22 ±0.02	3.0×10^{-3}	$(0.6\pm1.0)\times10^{-3}$	0.2± 0.3
				Total	1235.4±35.9

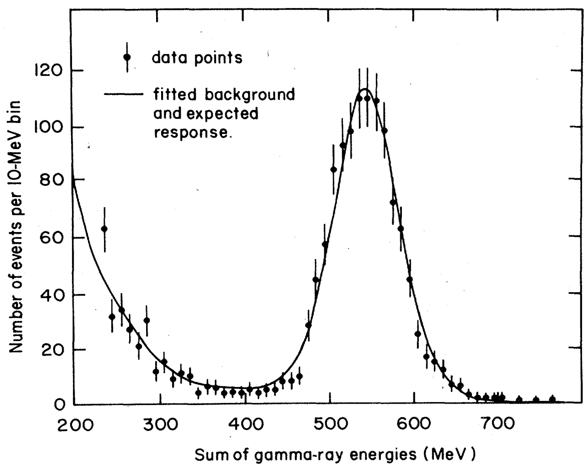

FIG. 18. Distribution of the sum of energies of coincident pairs of photons for class A events after final event selection. The fitted curve is the expected energy-response function plus a background shape based on the distribution of events selected only on the transverse-momentum parameter C.

B and C to class A gives confidence in the calculation of weights. Note that these numbers still contain the $\pi \rightarrow e\nu\gamma$ background.

The random background for each class was estimated by making a fit of a background spectrum shape plus the response function to the observed spectrum after all cuts. The background spectrum was obtained by using a spectrum with only the C cut applied, but with any real events (i.e., those passing final cuts) subtracted. Figures 18 and 19 show the fits for class A and classes B and C, respectively.

Finally the $\pi \rightarrow e\nu\gamma$ background is corrected for (see Sec. V A) to give the number of observed pion-beta-decay events

$$N_\beta = 1223.9 \pm 36.2 \; . \tag{6.12}$$

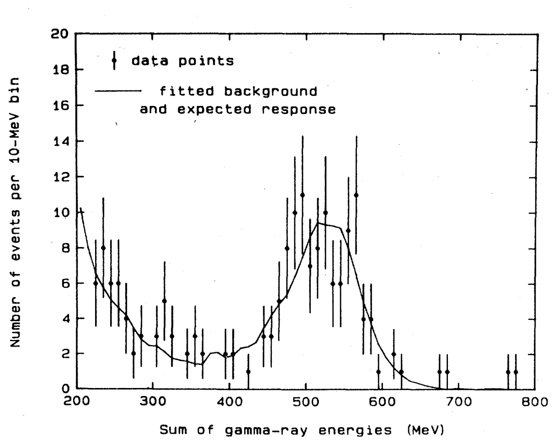

FIG. 19. Distribution of the sum of energies of coincident pairs of photons for class B and C events after final event selection. The fitted curve is the expected energy-response function plus a background shape based on the distribution of events selected only on the transverse-momentum parameter C.

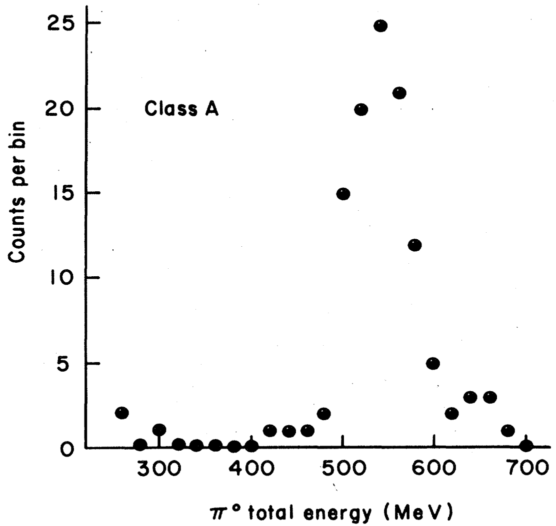

FIG. 20. Total energy spectrum of class A events with a coincident electron, selected only on χ_T^2.

VII. ANALYSIS OF THE PION-BETA-DECAY DATA WITH THE ELECTRON COUNTERS

The analysis of the pion-beta-decay data using information from the electron counters which were inside the vacuum tank is summarized here for completeness although it was not used in the determination of the pion-beta-decay rate.

The analysis was made from the SST's. In selecting the events, the following two basic cuts were first made on the data: χ_T^2 and fiducial-area cuts (class A events). The only other cut was to require one of the electron counters to fire in a time window 2.6 ns wide defining an $e\gamma\gamma$ coincidence. There were 119 such events. Figure 20 shows the π^0 total energy spectrum of the class A events selected by the electron counters. A peak is observed with a FWHM of $\Delta E = 75.5 \pm 8.2$ MeV centered at $E = 540.7 \pm 3.9$ MeV, corresponding to the detection of pion-beta-decay events and a few background events. Fitting a flat background to the electron-counter time distribution outside the 2.6 ns window gave for the number of background events inside the window

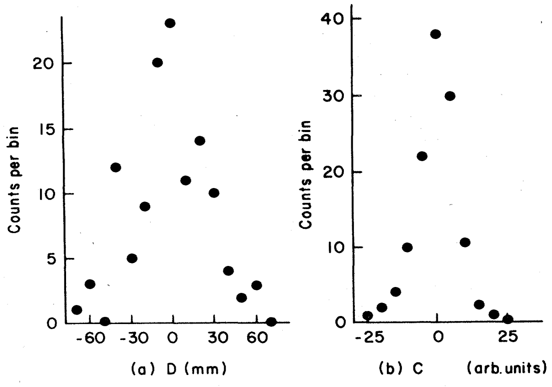

FIG. 21. Distribution of D and C parameters of selected class A events with a coincident electron.

$$N_R = 13.7 \pm 3.7 \ . \qquad (7.1)$$

The number N_A' of selected pion-beta-decay events was determined by subtracting N_R from the number of events (119) on the plot

$$N_A' = 105.3 \pm 10.4 \ . \qquad (7.2)$$

The uncertainty is statistical and includes the uncertainty in the background subtraction. This result can be compared with the corresponding number N_A of pion-beta-decay events to calculate a quantity X,

$$X = N_A' / N_A = (9.40 \pm 0.97)\% \ , \qquad (7.3)$$

where X is the relative proportion of pion-beta-decay events with the electron detected in one of the four electron counters. This quantity was also calculated in the Monte Carlo program PIOBETA by introducing in the code the geometry of the four electron counters and was determined as

$$X = (10.44 \pm 0.14)\% \ . \qquad (7.4)$$

The uncertainty is a combination of statistical errors and those due to uncertainties in the beam phase space, beam steering, and geometrical location of the detectors. Good agreement is noted between the experimental and Monte Carlo results.

For completeness, Figs. 21(a) and 21(b) show the D and C distributions, respectively, of the class A events selected by the electron counters. These two distributions are similar to the Monte Carlo and pion-beta-decay data-analysis distributions (see Figs. 16 and 17). The agreement between the energy distributions, and D and C distributions, of the events selected using the electron counters and those of events selected in the main analysis gives confidence in our assertion that these are real pion beta-decay events.

VIII. DISCUSSION

Using the data of Table IX, in Eq. (2.1), the final result for the pion-beta-decay rate is

$$R = (0.394 \pm 0.015) \ \mathrm{s}^{-1} \ , \qquad (8.1)$$

where the error includes statistical (3.1%) and systematic (2.0%) errors. Our result (8.1) is in good agreement with the standard-weak-interaction-theory prediction [Eq. (1.9)], the difference being $(-2.2 \pm 3.8)\%$, giving the best existing confirmation of the CVC hypothesis at low momentum transfer. Combining R with 26.030 ± 0.023 ns for the pion lifetime[9] gives a partial decay fraction of $(1.026 \pm 0.039) \times 10^{-8}$, to be compared to the result (1.10). The Kobayashi-Maskawa[22] model implies that the original Cabibbo approach[23] of using a single mixing angle for all beta decays is no longer appropriate,[24] and instead two angles are needed to parametrize $\Delta S = 1$ decays, with one of these used for $\Delta S = 0$ decays. Using the coupling constant for muon decay and assuming the validity of CVC and the radiative-correction calculation,[3] we obtain a ratio of 0.928 ± 0.035 between our result and the rate calculated without use of a mixing angle. The $\Delta S = 0$ mixing angle is then $\theta = 0.27^{+0.06}_{-0.08}$ rad (68% C.L.); in the context of the Weinberg-Salam-Kobayashi-Maskawa model this is the first direct measurement of this angle in a particle beta decay as opposed to a nuclear beta decay.

TABLE IX. Parameters entering into decay rate.

Symbol	Description	Value
N_β	Number of good events[a]	1223.9 ± 36.2
T	Time in decay region, s[b]	$(3.534 \pm 0.031) \times 10^{-11}$
N_π	Number of beam pions[b]	$(2.144 \pm 0.022) \times 10^{14}$
P^2	Conversion efficiency[a]	0.5151 ± 0.0062
F_1	Dalitz, early conversions[b]	0.9430 ± 0.0050
F_2	Trigger efficiency[b]	0.8917 ± 0.0090
F_3	Software efficiency[b]	0.9581 ± 0.0050
F_4	Event-selection efficiency[b]	0.9880 ± 0.0073

[a] Error is primarily statistical.

[b] Error in primarily systematic.

ACKNOWLEDGMENTS

We gratefully acknowledge the contribution of Kenneth W. Rothe to the original conception of the experiment and the assistance of J. D. Bowman and M. D. Cooper in adapting the π^0 spectrometer to this experiment. We also acknowledge the assistance of G. Hart, M. Dugan, E. Iverson, R. Sands, A. Waby, C. Burbach, and N. Haik, the engineering effort of C. F. Hansen and H. G. Worstell, and the support of the staff of LAMPF. One of the authors (F.C.G.) was given partial support by the Fonds National Suisse de la Recherche Scientifique. W.K.M. would like to thank CERN (EP Division) for its hospitality during the writing of this paper. This experiment was supported in part by the U.S. Department of Energy.

---

[*] Present address: CERN, Geneva, Switzerland.

[†] Present address: Fermilab, Batavia, IL 60510.

[1] W. K. McFarlane, L. B. Auerbach, F. C. Gaille, V. L. Highland, E. Jastrzembski, R. J. Macek, F. H. Cverna, C. M. Hoffman, G. E. Hogan, R. E. Morgado, J. C. Pratt, and R. D. Werbeck, Phys. Rev. Lett. **51**, 249 (1983).

[2] R. P. Feynman and M. Gell-Mann, Phys. Rev. **109**, 193 (1958).

[3] A. Sirlin, Rev. Mod. Phys. **50**, 573 (1978).

[4] G. Källén, *Elementary Particle Physics* (Addison-Wesley, Reading, Mass., 1964), p. 400ff.

[5] S. Weinberg, Phys. Rev. Lett. **19**, 1264 (1967); A. Salam, in *Elementary Particle Theory: Relativistic Groups and Analyticity (Nobel Symposium, No. 8)*, edited by N. Svartholm (Almqvist and Wiksell, Stockholm, 1968).

[6] D. H. Wilkinson and B. E. F. Macefield, Nucl. Phys. **A158**, 110 (1970).

[7] D. H. Wilkinson, A. Gallmann, and D. E. Alburger, Phys. Rev. C **18**, 401 (1978).

[8] I. S. Towner and J. C. Hardy, Phys. Lett. **73B**, 20 (1978).

[9] M. Roos *et al.* (Particle Data Group), Phys. Lett. **111B**, 1 (1982).

[10] P. Depommier, J. Duclos, J. Heintze, K. Kleinknecht, H. Rieseberg, and V. Soergel, Nucl. Phys. **B4**, 189 (1968). This includes a discussion of previous experiments.

[11] *LAMPF User's Handbook* [Los Alamos National Laboratory Report No. MP-DO-3-UHB (Rev.), 1984].

[12] B. Rossi, *High-Energy Particles* (Prentice-Hall, Englewood Cliffs, New Jersey, 1952).

[13] H. Messel and D. Crawford, *Electron-Photon Shower Distribution Function* (Pergamon, New York, 1970).

[14] H. W. Baer, R. D. Bolton, J. D. Bowman, M. D. Cooper, F. H. Cverna, R. H. Heffner, C. M. Hoffman, N. S. P. King, Jose Piffaretti, J. Alster, A. Doron, S. Gilad, M. A. Moinester, P. R. Bevington, and E. Winklemann, Nucl. Instrum. Methods **180**, 445 (1981).

[15] E. A. Wadlinger, Nucl. Instrum. Methods **134**, 243 (1976).

[16] W. J. Briscoe, D. H. Fitzgerald, B. M. K. Nefkens, and M. E. Sadler, Nucl. Instrum. Methods **197**, 277 (1982).

[17] D. L. Lind, B. C. Barish, R. J. Kurz, P. M. Ogden, and V. Perez-Mendez, Phys. Rev. **138**, B1509 (1965).

[18] S. Gilad, Ph.D. thesis, University of Tel-Aviv, 1979.

[19] A. Stetz, J. Carroll, D. Ortendahl, V. Perez-Mendez, G. Igo, N. Chirapatpimol, and M. A. Nasser, Nucl. Phys. **B138**, 285 (1978).

[20] D. E. Neville, Phys. Rev. **124**, 2037 (1961); D. A. Bryman, P. Depommier, and C. Leroy, Phys. Rep. **88**, 151 (1982).

[21] G. Källén, in *Springer Tracts in Modern Physics* (Springer, Berlin, 1968), Vol. 46, p. 67.

[22] M. Kobayashi and T. Maskawa, Prog. Theor. Phys. **49**, 652 (1973).

[23] N. Cabibbo, Phys. Rev. Lett. **10**, 531 (1963).

[24] R. E. Shrock and L.-L. Wang, Phys. Rev. Lett. **41**, 1692 (1978).